nature biomedical engineering

ARTICLES

PUBLISHED: 10 APRIL 2017 | VOLUME: 1 | ARTICLE NUMBER: 0054

Ultrasensitive tumour-penetrating nanosensors of protease activity

Ester J. Kwon[1,2†], Jaideep S. Dudani[1,3†] and Sangeeta N. Bhatia[1,2,4,5,6,7*]

The ability to identify cancer lesions with endogenous biomarkers is currently limited to tumours ~1 cm in diameter. We recently reported an exogenously administered tumour-penetrating nanosensor that sheds, in response to tumour-specific proteases, peptide fragments that can then be detected in the urine. Here, we report the optimization, informed by a pharmacokinetic mathematical model, of the surface presentation of the peptide substrates to both enhance on-target protease cleavage and minimize off-target cleavage, and of the functionalization of the nanosensors with tumour-penetrating ligands that engage active trafficking pathways to increase activation in the tumour microenvironment. The resulting nanosensor discriminated sub-5 mm lesions in human epithelial tumours and detected nodules with median diameters smaller than 2 mm in an orthotopic model of ovarian cancer. We also demonstrate enhanced receptor-dependent specificity of signal generation in the urine in an immunocompetent model of colorectal liver metastases, and *in situ* activation of the nanosensors in human tumour microarrays when re-engineered as fluorogenic zymography probes.

Early detection of tumours offers the hope of greatly improved outcomes for cancer patients[1]. For the majority of cancer types, diagnosis when the disease is localized to the organ of origin correlates with significantly greater long-term survival compared with when the disease has spread to distant sites, largely because currently available therapeutics are most effective when patients are treated in the early stages of disease[2–4]. Despite the need for technology that can detect early-stage disease, the predictive value of existing biomarkers used to diagnose cancers is limited. For example, recent studies have shown that screening with the blood biomarker CA-125 for ovarian cancer diagnosis does not improve patient outcomes[5]. However, screening with biomarkers that are predictive can significantly improve patient outcomes: colorectal cancer (CRC) mortality at 30-year follow-up was reduced by 32% with annual faecal occult-blood testing[6]. These studies indicate that more research is needed to develop biomarkers that are predictive of disease.

Despite the progress in improving tumour detection tools, clinical detection of tumours is limited to masses ~1 cm in diameter via imaging techniques (for example, magnetic resonance imaging (MRI) and positron emission tomography)[7,8] and analysis of blood biomarkers shed by the tumour (for example, proteins and cell-free nucleic acids)[8,9]. It is estimated that it can take up to ten years to establish tumours this size from the initial tumourigenesis[8], leaving a large window of opportunity for early diagnosis to improve patient outcomes. A minimally invasive tool to screen patients would significantly impact patient prognosis. To this end, we previously developed an exogenously administered activity-based nanosensor (ABN) that, in response to protease activity in the tumour, sheds peptide fragments that are ultimately concentrated in the urine[10,11]. Aberrantly expressed proteases are promising candidate enzymes to leverage in both diagnostics and therapeutics as they play critical roles in cancer progression[12]. While this ABN has shown promise for tumour detection in a subcutaneous flank model of CRC, a tool suitable for early detection would require order-of-magnitude gains in sensitivity.

Whereas the focus of conventional blood-based biomarkers is to identify specific signatures that act as barometers of the disease state and then to develop methods to sensitively detect them, our synthetic system has the advantage that it can be engineered to maximize both the specificity and the amplitude of analyte generation. A previously reported multi-compartment pharmacokinetic model (built on a system of ordinary differential equations) predicted that a 100-fold improvement in parameters related to tumour-specific signal generation would be necessary for detection of sub-5-mm-sized tumours[13]. Inspired and instructed by this model, we chose parameters to optimize our urinary diagnostic on the basis of the following design principles: detection of molecular events that are conserved hallmarks of tumour invasiveness, minimal interaction with the non-tumour host biology and robust sampling of the tumour microenvironment. We pursued two strategies, which we believed would act in synergy: (1) optimal proteolytic substrate presentation on the nanoparticle surface to maximize the relative on- versus off-target cleavage rates and (2) increased tumour access using tumour-penetrating ligands. Herein, we engineered our ABN platform using the above design criteria, and achieved detection of sub-5 mm tumour lesions in disease models that recapitulate important features of human disease. Furthermore, we demonstrated that our sensors respond to human cancer biopsy samples.

MMP9 is upregulated across human cancers

Our first objective was to engineer the ABN on the basis of a proteolytic target that is highly elevated across numerous human cancers

[1]Koch Institute for Integrative Cancer Research, Massachusetts Institute of Technology (MIT), Cambridge, Massachusetts 02139, USA. [2]Harvard–MIT Division of Health Sciences and Technology, Institute for Medical Engineering and Science, Massachusetts Institute of Technology, Cambridge, Massachusetts 02139, USA. [3]Department of Biological Engineering, Massachusetts Institute of Technology, Cambridge, Massachusetts 02139, USA. [4]Department of Electrical Engineering and Computer Science, Massachusetts Institute of Technology, Cambridge, Massachusetts 02139, USA. [5]Department of Medicine, Brigham and Women's Hospital and Harvard Medical School, Boston, Massachusetts 02115, USA. [6]Broad Institute of Massachusetts Institute of Technology and Harvard, Cambridge, Massachusetts 02139, USA. [7]Howard Hughes Medical Institute, Cambridge, Massachusetts 02139, USA. †These authors contributed equally to this work. *e-mail: sbhatia@mit.edu

and that has a fundamental biological role in tumour progression. Analysis of mRNA expression data from Oncomine (https://www.oncomine.org) and The Cancer Genome Atlas (TCGA; http://cancergenome.nih.gov) showed that matrix metalloproteinase 9 (*MMP9*) levels are significantly upregulated compared with control samples across many human cancer types (Fig. 1a), and can classify cancer as distinct from normal tissue, as established by constructing receiver operating characteristic (ROC) curves (median area under the curve (AUC) = 0.81; Fig. 1b). Furthermore, *MMP9* mRNA levels are consistent across all stages, indicating that it can be used for both early and late stage diagnosis (Supplementary Fig. 1a,b). Using MMP9 as a disease marker may be a valuable means to distinguish aggressive cancers from indolent ones, as it is known to play a critical role in the angiogenic switch needed for access to host vasculature when tumours reach 1–2 mm in diameter[14]. Therefore, MMP9 activity measurements may prospectively reflect disease progression, and not merely detect a byproduct of tumour growth, as is the case with many existing blood biomarkers.

We performed MMP9 immunohistochemical staining (blindly scored by a pathologist) on a tumour tissue microarray (TMA), and this confirmed that MMP9 protein levels were elevated across many human cancers (Fig. 1c–f and Supplementary Fig. 1c,d). Thus, on the basis of our analysis of human protein expression and the evidence in the literature[14,15], we proceeded to engineer our ABN as a probe for MMP9 activity *in vivo* and establish design principles that could be applied to other tumour-specific proteases found to be upregulated in cancer. Existing point-of-care technologies inadequately access MMP9, as it acts locally at the tumour site[14] and thus, may be challenging to assay from body fluids with high sensitivity and specificity[16]. Further exploration into other MMPs in breast cancer samples from TCGA revealed several other biomarker candidates that had elevated mRNA levels (Supplementary Fig. 1e). These proteases could be explored with multiplexed substrates in future iterations of the ABNs.

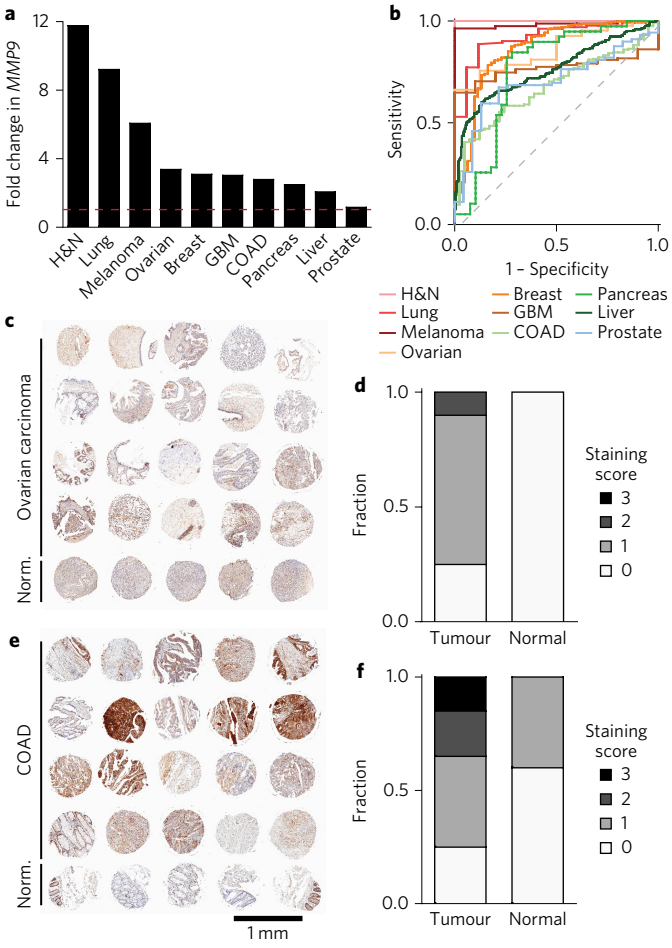

Figure 1 | MMP9 is upregulated across human cancers. a, Analysis of fold change in *MMP9* mRNA expression in tumours versus healthy controls; compiled from Oncomine and TCGA data. H&N, head and neck; GBM, glioblastoma multiforme; COAD, colorectal adenocarcinoma. Red dashed line indicates a fold change of 1. **b**, ROC curves constructed on the basis of *MMP9* mRNA expression data to represent how well MMP9 can classify various cancer types versus healthy controls (median AUC = 0.81). Grey dashed line represents a diagnostic with no discriminatory power (AUC = 0.50). **c**,**d**, Immunohistochemical staining of MMP9 protein in normal (Norm.) and ovarian carcinoma from a human TMA (**c**) and corresponding staining scores for tumour ($n = 20$ cores) versus normal ($n = 5$ cores) tissue (**d**). Blinded analysis of staining was performed by a pathologist; 3 for the highest level of staining and 0 for no visible staining. **e**,**f**, Immunohistochemical staining of MMP9 protein in normal colon and COAD from a TMA (**e**) and corresponding expression scores (**f**). Full TMA staining is shown in Supplementary Fig. 1d.

ABN optimization achieves order-of-magnitude improvement

We pursued two strategies to engineer an ultrasensitive nanosensor: (1) presentation of peptide substrates on the nanoparticle surface for maximal on-target and minimal off-target protease cleavage, and (2) modification of ABNs with tumour-penetrating ligands that engage active tumour trafficking pathways initiated by receptor binding. We hypothesized that these two strategies would cooperate to increase cancer-specific signal generation.

Extrapolating from experimental observations of enzyme–substrate interactions on monolayer surfaces[17], we hypothesized surface presentation would allow us to tune specificity between on- and off-target proteolytic cleavage rates of our MMP9 substrate. We tested the cleavage kinetics of an MMP9 peptide substrate (PLGVRGK)[10], flanked by a fluorescence resonance energy transfer (FRET) pair, at varying distances from our nanoparticle core (Fig. 2a). For this substrate, the rate of cleavage by MMP9 increased with increasing presentation distance (tether length) for all the substrate concentrations tested (0.5, 1.0, 2.0, 4.0 and 6.0 μM); as an example, cleavage velocity (V) increased from 0.24 to 0.96 nM s^{-1} at 6 μM (Fig. 2b). Unexpectedly, this phenomenon was not generalizable across enzymes: cleavage rates by the serine protease, thrombin, decreased with increasing presentation distance when the same substrate was tested (V at 6 μM of substrate decreased from 0.29 to 0.01 nM s^{-1}; Fig. 2c). Nor was it generalizable across substrates: thrombin cleavage of a thrombin-selective substrate (fPRSGGG; lower case letter indicates D-stereoisomer of the amino acid residue) was optimally presented at an intermediate length (Supplementary Fig. 2). Taken together, these data indicate that it is possible to significantly augment the signal-to-noise ratio of ABNs simply by tuning presentation on the nanoparticle surface (Fig. 2d). Optimizing substrate presentation is a possible solution to the challenge of engineering protease specificity for synthetic substrates[18,19], which has been relatively unexplored in the literature and could also be leveraged in other enzyme-activated technologies[20,21]. The presentation of the MMP9 substrate on our ABNs exploited the increased on-target and decreased off-target MMP9 cleavage that occurs for long tether lengths.

Next, we turned to the question of how to localize our MMP9 sensor so that it samples the tumour microenvironment in a living organism. Passive nanoparticle accumulation via the enhanced permeation and retention effect is heterogeneous in human tumours[22]; however, ligands can be deployed to improve the nanoparticle distribution in and around the tumour[23]. Although tumour-targeting ligands may not significantly affect overall bulk accumulation of nanomaterials in the tumour[23,24], they can increase cell-specific

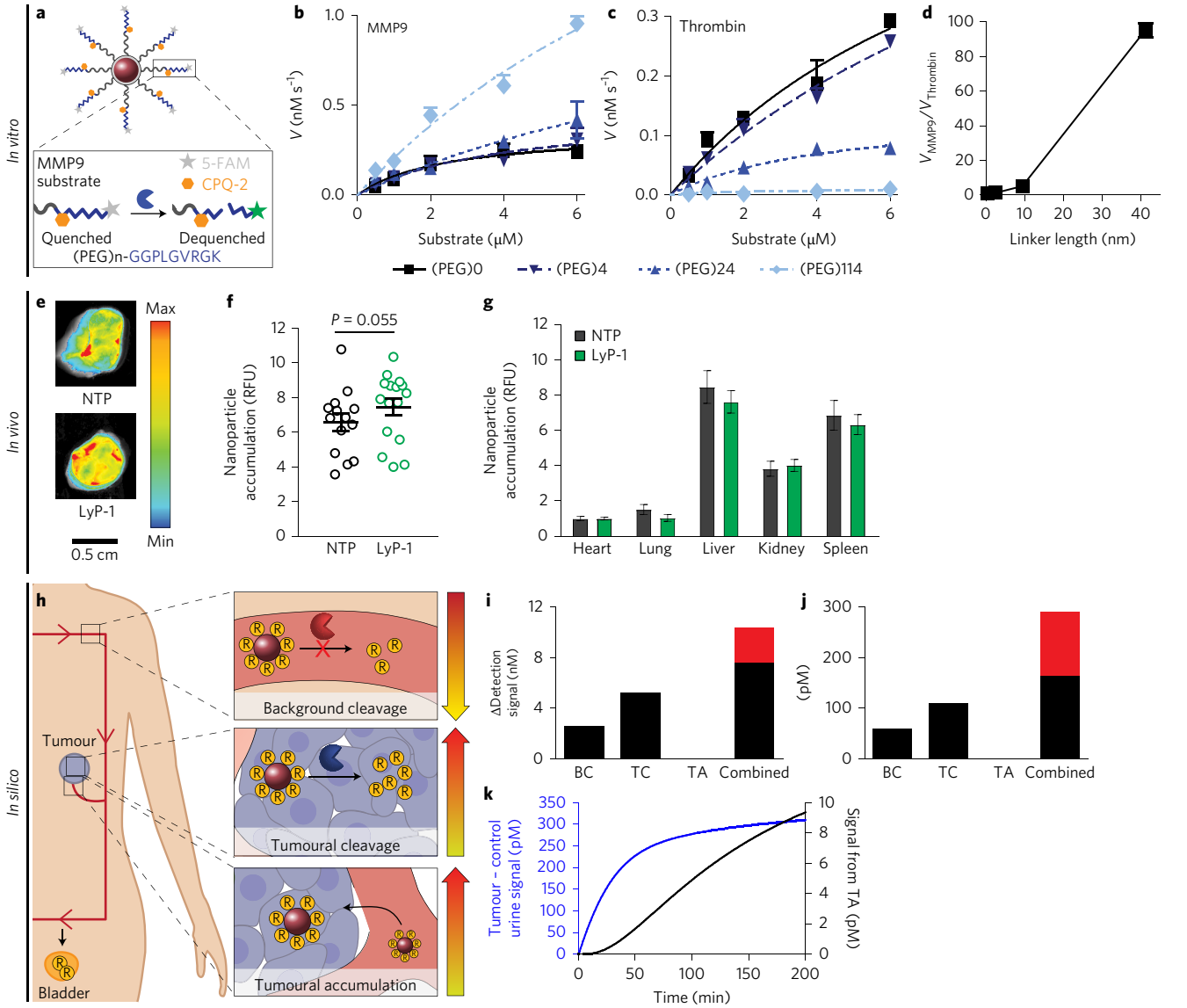

Figure 2 | *In vitro* and *in vivo* experiments and *in silico* evaluation enables engineering of an optimized ABN. a, Schematic showing FRET-based protease substrate displayed on an ABN surface. **b**,**c**, Cleavage velocity (*V*) of an MMP9 substrate by MMP9 (**b**) or thrombin (**c**) for 0, 4, 24 and 114 PEG subunits. Lines represent the fit to the Michaelis-Menten equation (mean ± s.e.m., $n = 2$–3). **d**, Ratio of MMP9 and thrombin velocities at a substrate concentration of 6 μM. **e**–**g**, Accumulation of LyP-1 ABNs and NTP ABNs (controls) in excised tumours (**e**) and quantification of ABN signal in tumours (**f**) and organs (**g**); mean ± s.e.m, $n = 7$ for NTP ABNs and $n = 8$ for Lyp-1 ABNs. RFU, relative fluorescence units. **h**, Schematic of parameters varied in a mathematical pharmacokinetic model. Encircled 'R's represent urine reporters. Arrows on the right indicate the direction in which the corresponding parameter was optimized to increase sensitivity. **i**,**j**, Change in detection signal when optimized parameters (BC, background cleavage; TC, tumoural cleavage; TA, tumoural accumulation) were applied to 10 mm (**i**) versus 5 mm (**j**) tumours (red denotes additional signal gained when parameters are combined, compared with the sum of the individual values for BC, TC and TA (BC+TC+TA)). **k**, Kinetic traces of the detected urine signal (tumour − control) with all three parameters optimized (blue line), and the contribution to the signal of increasing the TA term (black line).

association and retention in the tumour environment and positively impact clinical outcomes[25,26]. Furthermore, we hypothesized that the benefit of tissue-level localization is magnified when applied to an activity-based system, due to the synergy of the accumulation and enzymatic amplification effects. To this end, we employed a unique class of peptide ligands discovered by *in vivo* phage display that mediate active internalization and transport of nanomaterials past tumour stroma and into the tumour tissue; they are referred to as tumour-penetrating peptides[27,28].

We applied the dual strategy of optimizing MMP9-substrate presentation and increasing tumour-tissue access to our previously described urinary diagnostic platform[10]. We decorated our ABNs with the cyclic tumour-penetrating peptide, LyP-1 (CGNKRTRGC), previously shown to increase penetration of a variety of nanomaterials deep into the tumour parenchyma by binding its cognate receptor, p32, and engaging a secondary receptor, neuropilin-1 (NRP-1), which triggers an active transport pathway[29,30]. We employed an MDA-MB-435 subcutaneous flank xenograft as a model of an epithelial tumour. MDA-MB-435 tumours have elevated p32[31] and MMP9[32] expression. Non-tumour-penetrating (NTP) and LyP-1 ABNs were matched for substrate valency (Supplementary Fig. 3a,b) and were measured to have a ~60 nm hydrodynamic diameter and a slightly negative surface potential (Supplementary Fig. 3c). Visualization of their fluorescent cores three hours after administration revealed that the amount of ABN accumulation in the tumours was similar to that in organs (Fig. 2e–g); addition of LyP-1 moderately increased

tumoural accumulation (by ~20%) and resulted in slightly decreased off-target accumulation in organs, versus NTP ABNs (Fig. 2g).

We employed our previously developed pharmacokinetic mathematical model as a tool to understand how our improvements could affect the performance of the nanosensor[13]. The model comprises a set of five ordinary differential equations solved in three separate compartments (blood, tumour and bladder). The equations are derived from transport and biochemical governing equations (for example, Fick's Law and Michaelis-Menten kinetics) with variables fit to experimental data (Supplementary Text). On the basis of the *in vitro* and *in vivo* experimental ABN data presented above (Fig. 2a–g), we modified three parameters of the model: tumour-protease-specific cleavage (k_{cat}^{MMP9}), off-target cleavage ($k_{cat}^{background}$) and tumoural accumulation (k_{tumour}^{NP}) (K_{cat}, catalytic rate; NP, nanoparticle; Fig. 2h). When applied to tumours of moderate size (10 mm diameter), the model predicted cooperation between the three parameters: increases in detection signal were greater when parameters were input simultaneously compared with the sum of each parameter input individually (Fig. 2i, red bar). In fact, the model ascribed negligible enhancement of the detection signal to increased tumoural accumulation by itself. When we applied the same analysis to small tumours (5 mm diameter), similar trends were observed (Fig. 2j). The model predicted interactions between parameters to be greater for these smaller tumours, suggesting that multi-parameter optimizations are important when engineering ABNs for detection of small tumours. Lastly, we looked at the potential benefit of improved accumulation when combined with the other two parameters. This was assessed by measuring the difference in the detection signal when all three parameters were input versus when just the improved protease cleavage parameters were input (Fig. 2k). The model predicted only modest gains in urine signal. We hypothesized that the contribution from spatial distribution, tissue-level localization and overall changes in non-tumour biodistribution is greater than estimated. We therefore investigated performance of our optimized ABNs in a series of *in vivo* models with sub-5 mm tumours.

ABNs detect sub-5-mm tumours

To establish the minimum size of tumours that could be detected using the tumour-penetrating ABNs, a urinary test (measurement of peptide fragments in the urine 1 h after nanoparticle administration) was performed at 1, 2 and 3 weeks after initial tumourigenesis of MDA-MB-435 xenografts (Fig. 3a). Measurement of ABN half-life in the blood and substrate clearance in the blood and urine showed that the signal decayed rapidly, with half-lives being far shorter than the seven-day intervals between particle administrations (Supplementary Fig. 4a,b). At the time of each weekly urine test, we also measured the total tumour volume per mouse as determined by caliper measurements (Supplementary Fig. 5a–c). Non-penetrating ABNs with optimally presented MMP9 substrate discriminated tumours that were ~150 mm^3 in volume (Fig. 3b)—these volumes are approximately threefold smaller than those achieved when the substrate was directly presented on the nanoparticle surface[11]. Consistent with the *in silico* prediction that multi-parameter optimization would have a greater effect at small tumour sizes (Fig. 2j), the addition of tumour-penetrating ligands reduced the detection limit to tumour volumes between 20 and 50 mm^3, corresponding to tumour diameters of 3.4–4.6 mm (Fig. 3c). ROC analysis for tumour volumes of ≥50 mm^3 yielded an AUC of 0.83 for non-penetrating ABNs (Fig. 3d) compared with 0.95 for LyP-1 ABNs (Fig. 3e), indicating that LyP-1 increased the predictive power of our ABNs. Urine signals were also elevated when tracked over time (Supplementary Fig. 5d,e). The tumour-penetrating ligands markedly improved the urinary detection limit, reducing it from 150 mm^3 to 30 mm^3, despite their relatively moderate effect (1.2-fold increase) on accumulation. This unanticipated dramatic enhancement may be explained by biological phenomena such as cell- and tissue-level distribution, as observed previously in the literature[25,26]. Although this level of biological sophistication was not built into our model, because the study of nanoparticle–biological interactions is still an active area of research, our result demonstrates the value of molecular-targeting beyond simple measurements of bulk tissue accumulation[24] and highlights the need to develop our understanding of tumour localization. Taken together, optimization of substrate presentation and tumour-penetration improved the size limit for detectable tumours by over an order of magnitude (~14-fold), compared with limits of ~500 mm^3 for previous technology without these modifications[11].

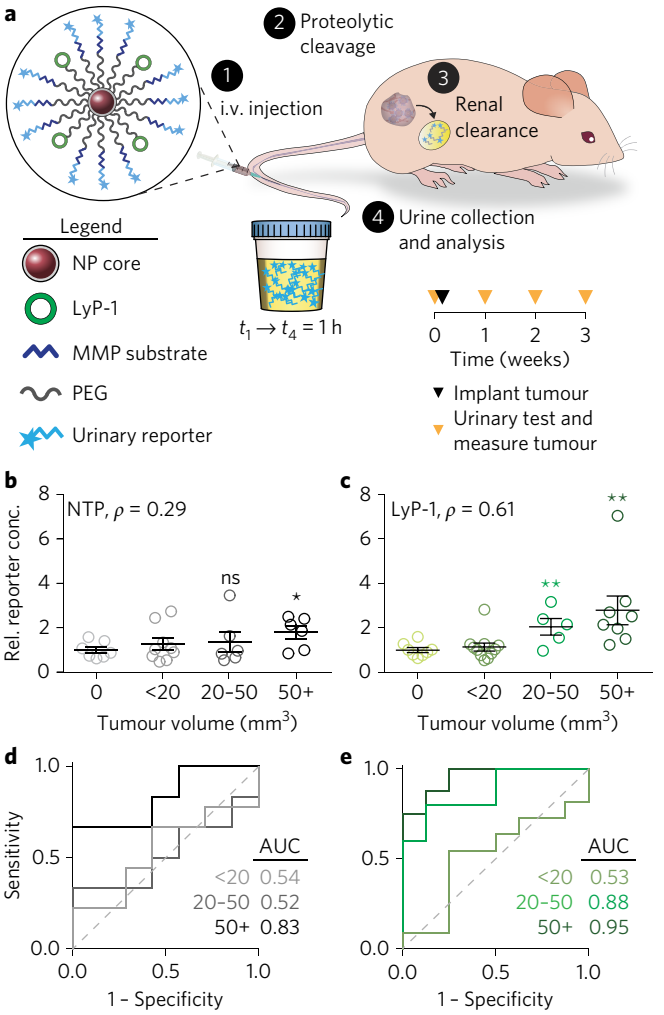

Figure 3 | Optimized ABNs detect sub-5 mm diameter tumours. **a**, Left and top: schematic showing urine testing in a mouse flank tumour (MDA-MB-435 xenograft) model. i.v., intravenous; *t*, time at given testing step (1–4). Bottom: study time line for urine testing. **b**,**c**, Relative reporter concentrations in the urine normalized to urine signal in healthy mice after administration of NTP ABNs (**b**; mean tumour size for 50+ bin, 146 mm^3) and LyP-1 ABNs (**c**; mean tumour size for 50+ bin, 132 mm^3). Tumours from seven (NTP ABNs) or eight (LyP-1 ABNs) mice measured over three weeks were binned by tumour size; mean ± s.e.m., two-tailed Student's *t*-test, $*P < 0.05$, $**P < 0.01$; ρ is the Spearman correlation between urine signal and tumour size in individual mice. For distribution of sizes, see Supplementary Fig. 4. **d**,**e**, ROC curves and calculated AUC values for NTP ABNs (control; **d**) and LyP-1 ABNs (**e**). Grey dashed line represents a diagnostic with no discriminatory power (AUC = 0.50).

ABNs outperform a clinical test in an ovarian cancer model

Early detection of ovarian cancer could yield substantial improvements in patient prognosis. Due to inadequate detection methods, 80% of current cases are diagnosed after the tumour has spread past

the ovary[33]. In addition, 70% of ovarian cancer patients relapse after being treated according to the standard of care, and therefore would greatly benefit from point-of-care longitudinal monitoring for early indications of relapse. On the basis of this clinical need, we challenged the tumour-penetrating ABN platform to detect a low tumour burden in an orthotopic disseminated xenograft model of high-grade serous ovarian cancer. The mouse model was established by intraperitoneal implantation of the human cell line OVCAR-8 (Fig. 4a), which displays surface p32[34] and NRP-1 (Fig. 4b), and secretes human epididymis protein (HE4)[35] (Supplementary Fig. 6a–c) and MMP9[36,37]. We confirmed that OVCAR-8 conditioned media can cleave the MMP9 substrate, which can be inhibited by the broad-spectrum matrix-metalloprotease inhibitor, marimistat (Supplementary Fig. 6d). Growth of tumours can be monitored by bioluminescence tracking of luciferized cells (Supplementary Fig. 6e,f). When implanted into the peritoneal space of mice, OVCAR-8 cells form disseminated tumour nodules (timescale of weeks) and the mice eventually accumulate ascites (timescale of months)—two disease presentations that also occur in human ovarian cancer patients. Two weeks after initial tumourigenesis, mice showed no overt signs of illness and had an average total tumour burden of 36 mm^3 with a median nodule diameter of <2 mm (Fig. 4c and Supplementary Fig. 7). After intravenous ABN administration, resected tumours showed significant accumulation of nanoparticles (Fig. 4d,e) and the total tumoural accumulation correlated strongly with tumour size (Supplementary Fig. 7a).

We tested whether our ABNs could: (1) detect low-burden ovarian cancer and (2) outperform a clinical blood biomarker. We chose to compare our system to the blood biomarker HE4 as OVCAR-8 cells produce relatively high levels of this protein, on a par with four other human ovarian cancer cell lines (Supplementary Fig. 6b,c). At a total tumour burden of 36 mm^3, the urinary signal from the ABNs was significantly elevated versus mice with no tumours (Fig. 4f). This threshold of sensitivity is critical, as clinically approved imaging modalities can typically only resolve individual tumour nodules greater than 5 mm in diameter. Additionally, in a retrospective analysis of clinical data, it has been estimated that to decrease serous ovarian cancer mortality by 50% with an annual screen, a test would have to be sensitive to tumours of <5 mm[38]. In contrast, the blood biomarker HE4 was not elevated to detectable levels at this timepoint and was only significantly elevated three weeks post-tumourigenesis, when the average total burden was 88 mm^3 (Fig. 4f and Supplementary Fig. 7b,c). A comparison of the two diagnostic systems' predictive powers indicated that ABN performance at two weeks (ROC-AUC = 0.99) exceeded that of HE4 at two weeks (ROC-AUC = 0.51) and three weeks (ROC-AUC = 0.93) (Fig. 4g). We confirmed that our tumour nodule retrieval methodology accounted for greater than 80% of the tumour burden by measuring luminescence pre- and post-resection (Supplementary Fig. 7d–g). The tumour burden remaining can be attributed to uncollected macroscopic and microscopic lesions.

The difference in the tumour volumes detected via an enzyme-linked immunosorbent assay (ELISA) of serum HE4 and those detected using the tumour-penetrating ABNs was 2.4-fold. It has previously been estimated that early stage human serous ovarian carcinomas have a doubling time of four months[38]. Extrapolating the benefit seen in detection compared with HE4 and assuming a simple monoexponential growth model of human ovarian cancer ($N_T(t) = N_{T0}e^{(\ln 2/[DT])t}$, where N_T is the starting tumour size and DT is the doubling time)[8], diagnosis could occur five months sooner for ABNs versus the blood biomarker. Improving diagnosis time by five months could significantly impact the prognosis of ovarian cancer patients, especially when it is considered that ovarian cancers spend an average of one year at stages III or IV before they become clinically apparent[38].

Ligand-receptor matching improves ABN urinary signal

Receptor expression on tumours varies by tumour type and patient. To engineer a nanosensor with versatile tumour-penetrating capabilities,

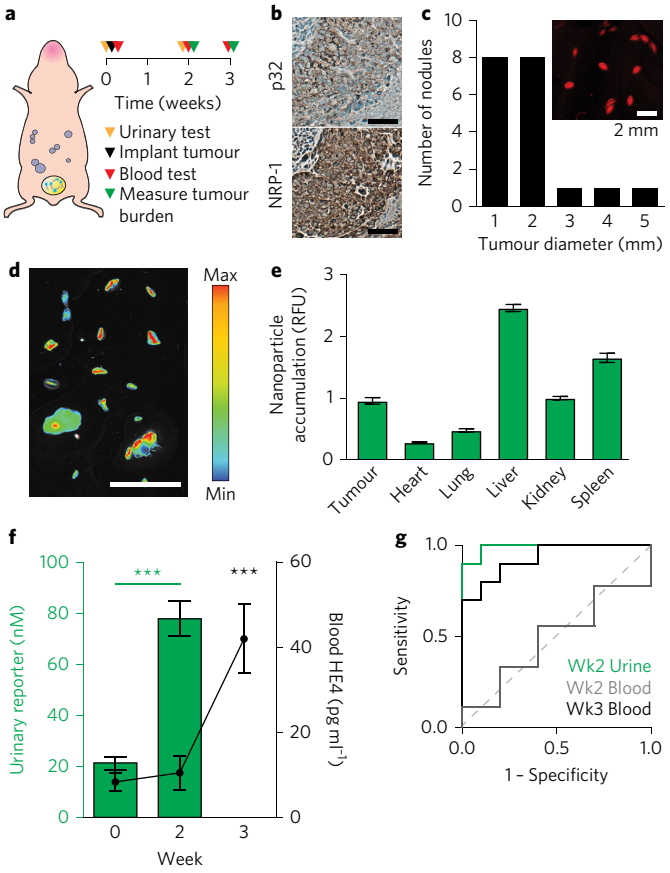

Figure 4 | Urinary biomarkers outperform blood biomarkers in detecting millimetre-sized lesions in orthotopic xenograft models of ovarian cancer. a, Schematic of LyP-1 ABN testing in an ovarian cancer model. **b**, Immunohistochemical staining of excised tumours (scale bars, 100 μm). **c**, Size distribution of tumour nodules retrieved from the intraperitoneal space of a representative animal two weeks after tumour initiation. Average total tumour burden at this timepoint was 36 mm^3 (Supplementary Fig. 6b, $n = 10$). **d**,**e**, Accumulation of ABNs in tumour nodules in a representative animal (**d**; scale bar, 1 cm) and biodistribution of ABNs in organs (**e**; mean ± s.e.m, $n = 10$). **f**, Urinary measurements of ABNs (green bars) and blood measurements of HE4 (black line); mean ± s.e.m, $n = 10$ per group, two-tailed Student's *t*-test, $^{***}P < 0.001$). **g**, ROC curve of urinary diagnostic and blood biomarker. Grey dashed line represents a diagnostic with no discriminatory power (AUC = 0.50).

we used another tumour-penetrating ligand, iRGD (CRGDKGPDC). This peptide engages the same active-internalization pathway as LyP-1, but binds to $\alpha_v\beta_3$ or $\alpha_v\beta_5$ integrin heterodimers as its primary receptor, which are ectopically overexpressed in a large subset of cancers[39,40](Fig. 5a). We applied iRGD and LyP-1 ABNs to an immunocompetent mouse model of colorectal liver metastasis (CLM), induced via an intrasplenic injection of p32-negative, integrin-positive and NRP-1-positive MC-26 cells (Fig. 5b,c and Supplementary Fig. 8a–c). MC-26 cells are derived from a mouse colorectal cancer line and secrete MMP9[41], which can be detected in the tumour nodules as well as in the tumour-adjacent liver, but not in non-tumour-bearing liver lobes (Fig. 5d). The stoichiometries for substrate conjugation on iRGD ABNs were similar to those used on the LyP-1 ABNs (Supplementary Fig. 9a). Mouse and human MMPs exhibit a high degree of homology[42], and we confirmed that mouse MMP9 cleaves our substrate (Supplementary Fig. 9b). A study of ABN clearance in immunocompetent BALB/c mice shows that no signal is detectable after 24 h in the urine, 48 h in the blood and 7 d in the tissues (Supplementary Fig. 10a–c). This was consistent in the model of

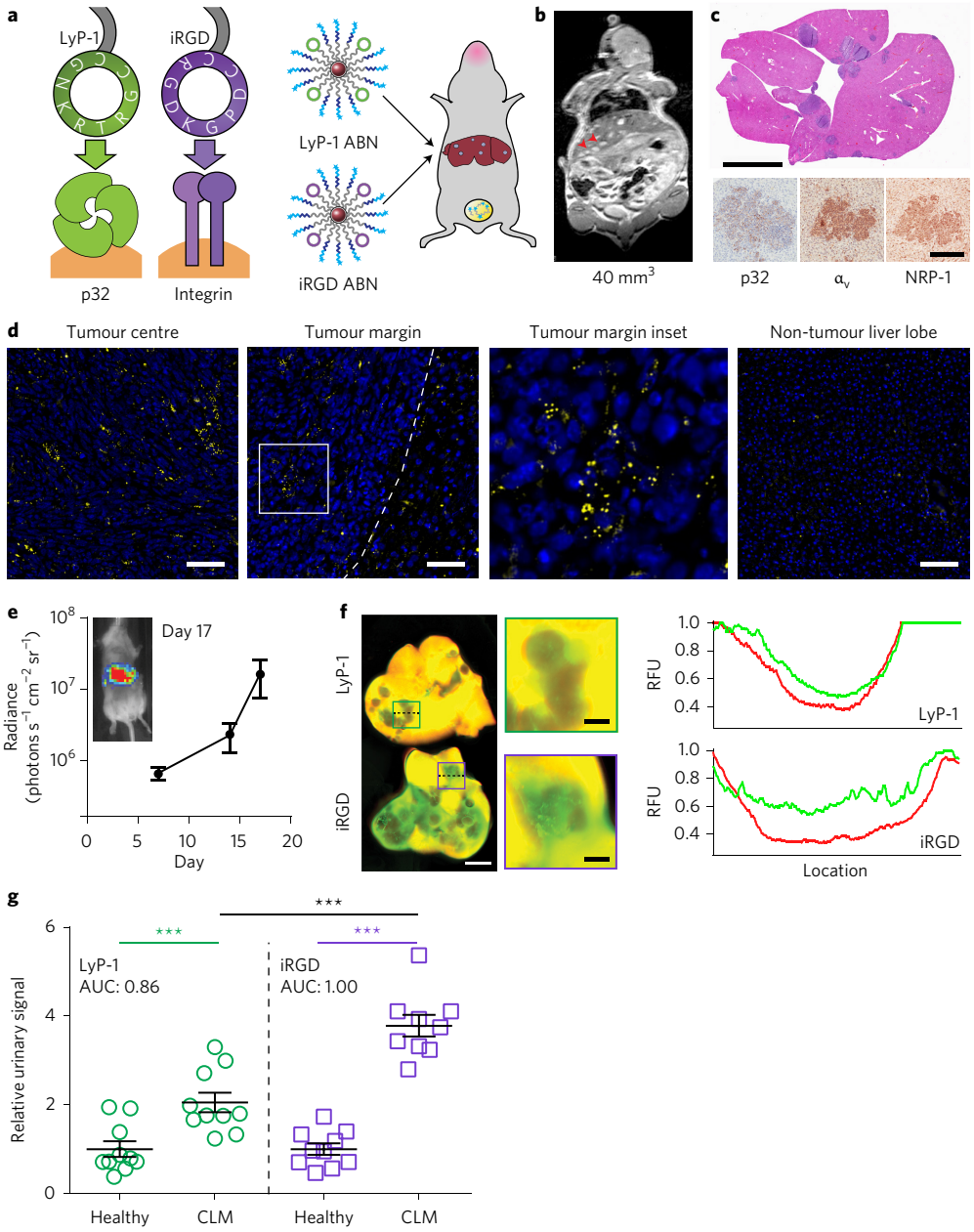

Figure 5 | Minimally invasive receptor classification of syngeneic liver metastasis via targeted ABNs. a, LyP-1 and iRGD both engage the same tumour trafficking pathway but rely on different primary receptors. LyP-1 and iRGD ABNs were tested in a liver metastasis model. **b**, MRI image of a CLM mouse with 40 mm^3 of total tumour burden; tumour nodules are indicated by red arrows. **c**, Top: haemotoxylin and eosin staining (scale bar, 5 mm). Bottom: immunohistochemical staining of tumour sections for the primary receptors, p32 and α_v integrin, and the secondary receptor, NRP-1 (scale bar, 200 µm). **d**, Imaging of tumour centre and margin, as well as normal liver, in sections from CLM mice. The tumour margin is indicated by a dashed line and the inset is indicated by a white box. Sections were stained for nuclei (blue) and MMP9 (yellow); scale bars, 100 µm. **e**, Bioluminescence imaging of CLM mice over time (mean ± s.e.m, $n = 20$). ABNs were administered when luminescence readings reached 10^7 photons s^{-1} cm^{-2} sr^{-1}. **f**, Left: fluorescent scans of tumours showing ABN accumulation (red, liver autofluorescence; green, nanoparticle; left scale bar, 2 cm; right scale bars, 5 mm). Right: line traces of ABN and liver autofluorescence (in relative fluorescence units) corresponding to the dashed lines. **g**, Relative reporter concentrations measured in the urine of healthy mice versus CLM mice after application of LyP-1 ABNs ($n = 10$ mice) or iRGD ABNs ($n = 9$ mice); the mean ± s.e.m is denoted by a horizontal line with error bars; two-tailed Student's t-test, $^{***}P < 0.001$.

orthotopic ovarian cancer (Supplementary Fig. 10d). Furthermore, no signs of toxicity were observed via histopathological assessment of tissues 3 h, 24 h and 7 d after ABN administration, when compared with PBS-injected controls (Supplementary Fig. 11).

The growth of individual liver metastases was measured by MRI and was well-correlated with the bioluminescence signal of luciferized MC-26 cells, allowing us to monitor total tumour burden via bioluminescence imaging (Fig. 5e and Supplementary Fig. 12). We examined nanoparticle localization after intravenous administration of iRGD or LyP-1 ABNs and observed no changes in overall nanoparticle accumulation across organs (Supplementary Fig. 13a), but increased penetration of iRGD ABNs into the tumour metastases compared with LyP-1 (Fig. 5f and Supplementary Fig. 13b,c). Application of either LyP-1 or iRGD ABNs in the urinary test resulted in distinct increases in signal when applied to mice with CLM compared with

healthy mice (Fig. 5g) and those that underwent sham surgeries (Supplementary Fig. 14). Consistent with low p32 and high integrin surface expression on MC-26 tumours (Fig. 5c), iRGD ABNs exhibited significantly improved diagnostic performance with relative reporter-concentration increases that were greater than those for LyP-1 ABNs (AUC = 1.00 versus 0.86, respectively). The urine signal was also more positively correlated with overall burden for iRGD versus LyP-1 ABNs (Supplementary Fig. 14b). As might be anticipated from low p32 surface expression in MC-26 tumours, administration of LyP-1 ABNs to CLM mice resulted in relative reporter-concentration increases similar to those for non-penetrating ABNs administered in the hind flank model (Fig. 3b), thereby supporting the idea that matching the ligand to the primary receptor can enhance the urinary signal. ABNs could serve as a minimally invasive modality to monitor patients longitudinally after primary tumour resection in colorectal cancer, where the majority of patients are at risk of developing CLM[3].

ABN zymography evaluates substrates in human tissues

With the long-term goal of translation into patients, we set out to validate the response of our sensors in human samples. However, the evaluation and localization of protease activity on synthetic peptide substrates in excised tissues has been challenging because substrates can diffuse away after proteolysis[43]. To investigate ABN activity in *ex vivo* tissues, we applied a FRET-pair flanked substrate such that cleavage could be monitored with fluorescence imaging (Fig. 6a). Combining existing zymography techniques[44] with our ABNs (henceforth, referred to as ABNz) allowed the mapping of protease activity to tissue localization. Here, the critical step involved binding the nanoparticle to the tissue before proteolysis occurred, thereby enabling localization. When iRGD ABNz was applied to frozen liver metastasis sections from CLM mice, the signal was dependent on both MMP activity, which was reduced by pharmacological inhibition, and binding, which was reduced when divalent cations necessary for integrin receptor engagement were omitted (Fig. 6a).

Lastly, we applied iRGD ABNz to a frozen human CRC TMA that contained biopsies from tumours and normal adjacent tissue (Fig. 6b). The extent of signal colocalization for activated ABNz, integrin and MMP9 in the cells of each tissue core was blindly scored. The results indicated that ABNz responded differently to tumour tissue compared with normal adjacent tissue, with 9 of 20 tumour cores showing a high signal, compared with only 3 of the 20 normal cores (Fig. 6c). We note that the normal adjacent tissues were collected from CRC patients and may have had elevated protease levels compared with tissue from healthy patients. A closer examination of the tissue (Fig. 6d,e) showed examples of ABNz activation co-localizing with integrin and MMP9 staining. The finding that ABN-based signal generation correlates with MMP9 and integrin expression in human tissues supports the applicability of this platform to the detection of human cancers. Beyond this application, our technology could also be used as a tool to profile human tissues for spatial information on protease activity that could support the translation of other protease-sensitive technologies and therapeutics.

Outlook

To extend the ABN technology for application to a wide selection of tumours, a suite of tumour-penetrating ligands specific for a range of primary receptors could be built by incorporation of the C-end rule motif, K/RXXK/R, which triggers the active internalization pathway[28]. Recent investigation into the mechanisms of these ligands implicates trafficking pathways distinct from endocytosis[30]. In this work, we employed two peptides, LyP-1 and iRGD, which bind to different primary receptors, but use the same NRP-1 secondary receptor to initiate tumour penetration[31,45]. In particular, the

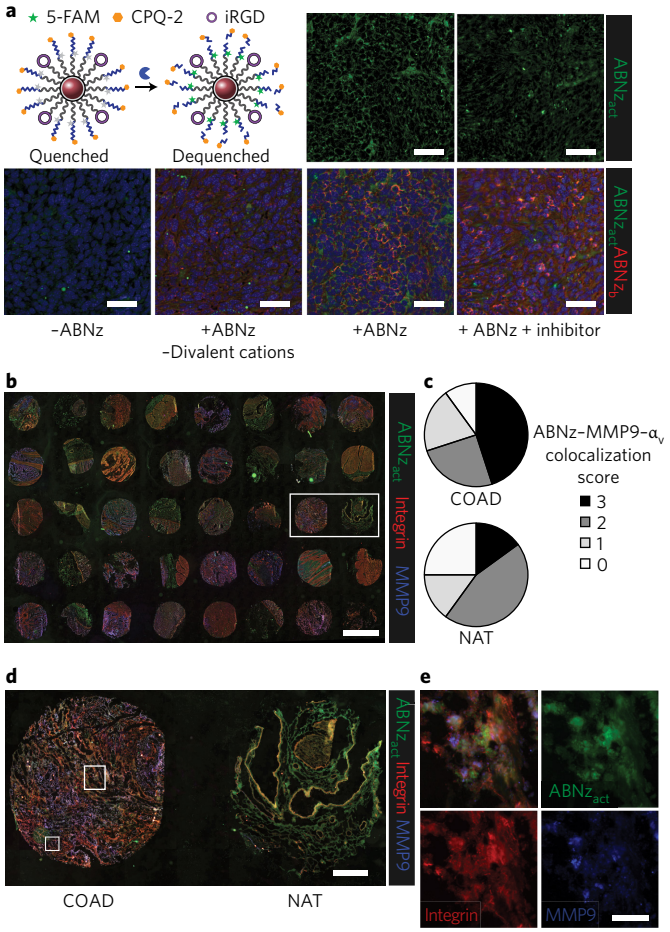

Figure 6 | ABN zymography is responsive to human tissues. a, Top left: schematic of ABNs re-engineered for zymography (ABNz). Nanoparticles were modified with iRGD targeting ligands and FRET-pair flanked substrates that increase their fluorescence on proteolytic cleavage. Frozen sections of CLM livers collected from mice were bound with PBS only (−ABNz), ABNz without divalent cations necessary for iRGD binding, and ABNz. Tissues were subsequently cleaved in MMP9 buffer with and without MMP9 inhibitor and imaged for the bound ABNz ($ABNz_b$: red) and cleaved ABNz ($ABNz_{act}$: green); scale bars, 50 μm. **b**, Application of iRGD ABNz to a human CRC tumour microarray consisting of 20 colorectal adenocarcinoma (COAD) samples and 20 normal adjacent tissue (NAT) (scale bar, 2 mm). **c**, Extent of signal colocalization between COAD and NAT samples scored on a scale of 0 to 3 by a blinded independent researcher. **d**, Higher-magnification image of the boxed area in **b** showing a patient sample containing cancer (left) and normal adjacent tissue (right); scale bar, 400 μm. **e**, Magnified tissue from boxed area in **d** showing cell-level colocalization of activated ABNz with integrin and MMP9 staining (scale bar, 40 μm).

iRGD peptide has been shown to increase the accumulation and activity of the therapeutic antibody, trastuzumab[45]. We note that the target of trastuzumab is extracellular human epidermal growth factor receptor 2 (HER2), which supports our use of these peptides to sense extracellular MMP9. Furthermore, a corollary to the observation that the urinary signal increases when primary receptor is matched with the tumour-penetrating ligand is that this technology can be further developed as a cocktail of tumour-penetrating ABNs to noninvasively and rapidly stratify patients on the basis of receptor expression. This tool could be used as a companion diagnostic to monitor receptor status in tumours treated with precision medicines, such as integrin-targeted therapeutics.

To move this technology towards potential clinical translation, we validated the response of our ABN technology to human tumour biopsy samples. We benchmarked the technology against the blood biomarker HE4, which has been shown to perform well in detecting early stage ovarian cancer[46]. Our technology was able to outperform HE4, detecting orthotopic tumour volumes that were 2.4-fold lower. On the basis of simple monoexponential growth models[8], this would allow the ABNs to provide a diagnosis five months earlier than the measurement of HE4. We also note that the median ovarian cancer nodule diameter detected by transvaginal ultrasound in humans is 4.7 cm, a tumour volume that is ~1,500 times larger than the volume that we detected in our orthotopic mouse model[47]. Nonetheless, it is unclear how the detection limit in the mouse models will scale to human tumour detection. While both pre-clinical and clinical characterization and development will be necessary to apply this technology for the detection of small tumour lesions in humans, recent translational work in protease-activated imaging has shown promise from mouse models to human clinical trials and outlines a path for application in patients[26]. Looking forward, further improvement in protease-based cancer detection technology can be made as new cancer-specific protease profiles and specific substrates are identified. Our approaches to engineering an ultrasensitive diagnostic tool can be coupled with the specificity achieved through multiplexing of protease substrates[10] and targeting ligands.

Methods

MMP9 expression analysis. MMP9 expression data was queried from Oncomine and TCGA where transcriptomic data were available for both tumour and control samples. The list of cancers analysed can be found in the Supplementary Information. Expression in tumours was normalized to controls from each data set.

Tissue microarray staining and scoring. A multiple-organ cancer and normal-tissue microarray was obtained from US Biomax (MC5003b). The microarray was stained with anti-MMP9 antibodies (Abcam; 1:1,000). Blind scoring of cores was performed by a pathologist.

Synthesis of peptides and nanoparticles. All peptides were synthesized by CPC Scientific. For recombinant enzyme studies and ABNz, intramolecularly quenched peptides were used: MMP substrate, 5-FAM–GGPLGVRGKK(CPQ2)–PEG2–C; thrombin substrate, 5-FAM–GGfPRSGGGK(CPQ2)–PEG2–C; where 5-FAM is the 5-carboxyfluorescein fluorophore, CPQ2 is the quencher, PEG2 is the linker polyethylene glycol, and lower case letters indicate the D-stereoisomer of the residue. *In vivo* protease-sensitive substrates were synthesized to contain a urinary reporter comprised of a protease-resistant D-stereoisomer of glutamate-fibrinopeptide B with a near-infrared dye for urinary detection (biotin–CGPLGVRGKK(Cy7)eGvndneeGffsar; Cy7 is cyanine7). Targeting peptides were synthesized and cyclized: LyP1, C–K(5-FAM)–C6–CGNKRTRGC; iRGD, C–PEG2–CRGDKGPDC; where C6 is the 6-aminohexanoic acid linker and there is a disulfide bridge between Cysteines 2 and 3.

Iron-oxide nanoparticles were formed by reacting iron(III) chloride hexahydrate and iron(II) chloride tetrahydrate with dextran as previously described[48]. These nanoparticles have been previously shown to be biocompatible and safe, and were cleared from the animal within five days[10]. Nanoparticles were aminated by reaction with ammonium hydroxide. Size measurements were performed by dynamic light scattering (Malvern Instruments Nano ZS90). For conjugation of peptides to NPs, the NPs were first reacted with NHS-VivoTag 680 (VT680, Perkin Elmer) and MAL-PEG(5k)-SVA (Laysan Bio) to introduce sulfhydryl reactive handles. Cysteine-terminated peptides were then reacted with the NPs and unreacted peptide was filtered using spin filters (molecular weight cut-off, 30 kDa; Millipore). For experiments to identify optimal PEG lengths, PEG of varying lengths was purchased (Thermo Fisher) and reacted in the same manner. Nanoparticles were stored in PBS at 4 °C or at −20 °C. Valencies of peptide conjugation and concentrations were quantified by absorbance (Molecular Devices SpectraMax Plus). Typical valencies were ~60 protease-cleavable peptides, ~5 targeting peptides and ~10 VT680s per nanoparticle.

***In vitro* recombinant protease assays.** Nanoparticles coupled with intramolecularly quenched peptide substrates were reacted with recombinant proteases to identify cleavage velocities. NPs were mixed with 1% (w/v) BSA (Sigma) and incubated with recombinant proteases (MMP-9, Enzo Life Sciences; thrombin, Haematologic Technologies) in a final volume of 50 µl in enzyme-specific buffers (MMP9 buffer: 50 mM Tris, 150 mM NaCl, 5 mM $CaCl_2$, 1 µM $ZnCl_2$, pH 7.5; thrombin: PBS) in a 384-well plate for time-lapse fluorimetry to measure dequenching at 37 °C (SpectroMax Gemini EM microplate reader). Michaelis-Menten constants were determined by assessing initial cleavage velocities at different substrate concentrations (Prism 5.0, GraphPad). The final MMP-9 concentration was 100 nM and the final thrombin concentration was 7 nM.

Cell culture. The MDA-MB-435 human cancer cell line (American Type Culture Collection) and MC-26 (Tanabe Laboratory, Massuchusetts General Hospital) mouse colon carcinoma cell line were cultured in Dulbecco's modified Eagle medium supplemented with 10% foetal bovine serum and 1% penicillin–streptomycin. The OVCAR-8 human ovarian cancer cell line (National Cancer Institute 60 Human Tumor Cell Lines Screen) was cultured in Roswell Park Memorial Institute medium supplemented with 10% foetal bovine serum and 1% penicillin–streptomycin. All cell lines used in these studies were obtained from the sources given above (no additional identification procedures were performed), and all tested for mycoplasma.

Antibody staining and flow cytometry. To confirm the expression of targetable integrins on the MC-26 cells, cells were collected with enzyme-free cell-dissociation buffer (Thermo Fisher). Cells were stained for α_v integrin (550024, BD Pharmingen; 1:100), NRP-1 (AF566, R&D Biosystems; 1:100), and p32 (AB 2991, Millipore; 1:100) at 4 °C for 1 h and then probed with secondary antibodies conjugated to fluorophores according to manufacturer's instructions. Cells were analysed by flow cytometry on a BD LSR II flow cytometer.

ELISA for ovarian cancer blood biomarkers. Secreted and cytoplasmic levels of HE4 were measured by ELISA, according to the manufacturer's protocol (R&D Systems). Cultured supernatant and lysed cells from five cell lines were diluted as needed. All measurements were normalized to the number of cells and the secretion time.

MDA-MB-435 subcutaneous xenograft studies. All animal studies were approved by the Massachusetts Institute of Technology (MIT) committee on animal care (MIT protocol 0411-036-14). To generate subcutaneous grafts, three- to four-week-old female NCr nude mice (Taconic) were injected bilaterally with 5×10^6 MDA-MB-435 cells per flank. Urine measurements were made prior to tumour inoculation by intravenously injecting either 0.5 µM LyP1 or NTP ABNs (concentrations determined by protease substrate) in 200 µl of PBS at weekly intervals after inoculation. After nanoparticle injection, mice were placed in custom housing with a 96-well plate base for urine collection. After 1 h, their bladders were voided to collect between 100–200 µl of urine. For analysis, urine was diluted between 10- and 25-fold in PBS. Urine reporter concentration was quantified by measurement of Cy7 fluorescence using a LI-COR Odyssey infrared imaging system (with reference to a ladder of known reporter concentrations). Tumour sizes were measured using digital electronic calipers (Marathon Management) and their volume was calculated as $0.5\times\text{length}\times\text{width}^2$, where length and width are the larger and smaller dimensions, respectively. Total tumour volume was defined as the sum of the tumour volume in each flank. Mice were binned on the basis of tumour sizes and the urine signal was quantified for these bins. ROC curves were generated using Prism.

For NP quantification and determination of the NP distribution in organs and tumours, mice were killed 3 h after the NP injection, and the organs were removed and scanned in the LI-COR Odyssey. Fluorescence from the nanoparticle scaffold (VT680) and the peptide (Cy7) was quantified using the ImageJ software package (National Institutes of Health).

Pharmacokinetic mathematical model. For a complete description and derivation of the model, refer to ref. [13]. We inputted the measured properties of our sensor by modifying the base case values from the previous model. From the data shown in Fig. 2a–g, MMP9 cleavage was found to increase 4-fold for 6 µM of substrate and thrombin cleavage decreased 29.1-fold at the same substrate concentration. We used these numbers and inputted them to change the base case values for k_{cat}^{tumour} and $k_{cat}^{background}$ by the respective fold changes observed. Here, we assume the change in thrombin cleavage is abstracted to background proteolysis for simplicity. From the data shown in Fig. 2g, it can be seen that tumoural accumulation increased 1.2-fold. We updated the permeability term k_{np_tumour} in the ordinary differential equation by the observed difference. We further modified the nanoparticle half-life to match that of our nanosensors. For the 10 mm tumour, we used the base case model tumour-enzyme concentration of 700 nM, and for the 5 mm tumour, we used a concentration of 7 nM, which is in the range observed for tumours of this size.

Ovarian cancer orthotopic model studies. To generate an orthotopic model of human ovarian cancer, three- to four-week-old female NCr nude mice were injected intraperitoneally with 2×10^6 OVCAR-8 cells expressing firefly luciferase. Tumour burden was measured via luminescence using an *in vivo* imaging system (IVIS, PerkinElmer). Each mouse was killed and the tumours were retrieved from all organs in the peritoneal space. Tumours were collected on a glass slide and scanned on a LI-COR Odyssey with 169 µm resolution. Widths and lengths were

measured with ImageJ and tumour volume was calculated as described above for subcutaneous tumours. The reported tumour volumes for each group are the average of ten mice. The size distribution of nodules recovered from each mouse is shown in Supplementary Fig. 7c. Before tumour induction, urine measurements were performed by injecting mice with 0.5 µM LyP1 ABNs as described above.

Approximately 200 µl of blood was collected and spiked with EDTA to a final concentration of 5 mM and the blood cells were pelleted. Plasma was stored at −20 °C prior to HE4 quantification. HE4 levels were measured using the HE4 quantikine ELISA kit according to the manufacturer's protocol (R&D Systems).

Liver metastasis model studies. Immunocompetent six- to eight-week-old female BALB/c mice were injected with 5×10^4 syngeneic MC-26 cells expressing firefly luciferase in the subsplenic capsule to allow cells to seed the liver. After 90 s, the spleen was removed to prevent splenic tumours. Tumour growth was monitored by luminescence and MRI. Before induction of liver metastases, urine measurements were made by injecting 0.5 µM iRGD or LyP-1 ABN biomarkers. Post-tumour inoculation urine measurements were performed when tumour luminescence reached an average of $1–1.5\times10^7$ photons s^{-1} cm^{-2} sr^{-1}.

Toxicity and clearance studies. All studies were completed in immunocompetent six- to eight-week-old female BALB/c mice. After administration of ABNs or free reporter, 10 µl of blood and urine were collected at the indicated timepoints for fluorescence measurements. For tissue clearance and histopathological examination, animals were killed at the indicated timepoints and their organs were fixed in formalin. Organs were imaged for ABNs with the LI-COR Odyssey as described above, before being embedded in paraffin and then sectioned.

Histology. All histology sectioning and staining was performed at the Koch Institute Histology Core. Immediately after necropsy, the organs were fixed in formalin for 24 h and stored at 4 °C, before being embedded in paraffin, sectioned and stained. OVCAR-8 tumour sections were stained with p32 (Genscript custom antibody; 1:100) and NRP-1 (AF3870, R&D Biosystems; 1:100). MC-26 tumour sections were stained with α_v integrin (AB1930, Millipore; 1:100), p32 (AB2991, Millipore; 1:100) and NRP-1 (AF566, R&D Biosystems; 1:100).

Application of ABNz. Livers from CLM mice were extracted and immediately embedded and frozen in optimal-cutting-temperature compound. Before application of ABNz, liver sections were air dried and fixed in cold acetone[44]. Protease substrates were designed in a similar manner to the intramolecularly quenched probes used in the *in vitro* cleavage experiments, except that the fluorophore and quencher positions were reversed. A fresh frozen acetone-fixed human CRC TMA was purchased from US Biomax (FCO405a). After hydration in PBS and blocking in 2% BSA solution for 1 h at 4 °C, ABNz was applied and the microarray was incubated for 3 h at 4 °C with and without divalent cations in the buffer to allow for binding but no cleavage. The slide was washed and the buffer was exchanged with MMP9 cleavage buffer (recipe above) and incubated at 37 °C overnight in a humidified box. For inhibited controls, 50 µM marimastat was added to the binding and cleavage buffers. Slides were stained with α_v integrin (327902, BioLegend; 1:100) and MMP9 (137867, Abcam ab; 1:500) followed by application of the appropriate secondary antibodies (Jackson Immunolabs). Slides were scanned on a Pannoramic 250 Optimum (PerkinElmer) and co-localization was scored blindly by an independent researcher.

Statistical analyses. All statistical analyses were performed using GraphPad Prism 5.0 or MATLAB R2013b. Each set of data shown is representative of studies repeated in at least two independent experiments. The sample sizes used for animal experiments ($n=7–10$) were estimated using a power test with an expected effect size of 50–100% and a variance of 30–50%. No animals were excluded from the analyses. The investigators were not blinded to the groups and treatments during the experiments. For each animal experiment, groups were established before tumourigenesis and therefore no randomization was used in the allocation of groups.

Code availability. Skeleton MATLAB code of the pharmacokinetic model is available on GitHub at https://github.com/jaidud3/Cancer-activity-based-nanosensor-mathematical-framework.

Data availability. The authors declare that all data supporting the findings of this study are available in the paper and its Supplementary Information.

Received 14 August 2016; accepted 1 March 2017; published 10 April 2017

References

1. Etzioni, R. *et al.* The case for early detection. *Nat. Rev. Cancer* **3,** 243–252 (2003).
2. *SEER Cancer Statistics Review, 1975–2013* (National Cancer Institute, 2016); http://seer.cancer.gov/csr/1975_2013
3. Kanas, G. P. *et al.* Survival after liver resection in metastatic colorectal cancer: review and meta-analysis of prognostic factors. *Clin. Epidemiol.* **4,** 283–301 (2012).
4. Bristow, R. E., Tomacruz, R. S., Armstrong, D. K., Trimble, E. L. & Montz, F. J. Survival effect of maximal cytoreductive surgery for advanced ovarian carcinoma during the platinum era: a meta-analysis. *J. Clin. Oncol.* **20,** 1248–1259 (2002).
5. Fader, A. N. *et al.* The prognostic significance of pre- and post-treatment CA-125 in grade 1 serous ovarian carcinoma: a gynecologic Oncology Group study. *Gynecol. Oncol.* **132,** 560–565 (2014).
6. Shaukat, A. *et al.* Long-term mortality after screening for colorectal cancer. *N. Engl. J. Med.* **369,** 1106–1114 (2013).
7. Frangioni, J. V. New technologies for human cancer imaging. *J. Clin. Oncol.* **26,** 4012–4021 (2008).
8. Hori, S. S. & Gambhir, S. S. Mathematical model identifies blood biomarker-based early cancer detection strategies and limitations. *Sci. Transl. Med.* **3,** 109ra116 (2011).
9. Henry, N. L. & Hayes, D. F. Cancer biomarkers. *Mol. Oncol.* **6,** 140–146 (2012).
10. Kwong, G. A. *et al.* Mass-encoded synthetic biomarkers for multiplexed urinary monitoring of disease. *Nat. Biotechnol.* **31,** 63–70 (2013).
11. Warren, A. D., Kwong, G. A., Wood, D. K., Lin, K. Y. & Bhatia, S. N. Point-of-care diagnostics for noncommunicable diseases using synthetic urinary biomarkers and paper microfluidics. *Proc. Natl Acad. Sci. USA* **111,** 3671–3676 (2014).
12. Koblinski, J. E., Ahram, M. & Sloane, B. F. Unraveling the role of proteases in cancer. *Clin. Chim. Acta* **291,** 113–135 (2000).
13. Kwong, G. A. *et al.* Mathematical framework for activity-based cancer biomarkers. *Proc. Natl Acad. Sci. USA* **112,** 12627–12632 (2015).
14. Kessenbrock, K., Plaks, V. & Werb, Z. Matrix metalloproteinases: regulators of the tumor microenvironment. *Cell* **141,** 52–67 (2010).
15. Farina, A. R. & Mackay, A. R. Gelatinase B/MMP-9 in tumour pathogenesis and progression. *Cancers* **6,** 240–296 (2014).
16. Wu, Z.-S. *et al.* Prognostic significance of MMP-9 and TIMP-1 serum and tissue expression in breast cancer. *Int. J. Cancer* **122,** 2050–2056 (2008).
17. Deere, J. *et al.* Kinetics of enzyme attack on substrates covalently attached to solid surfaces: influence of spacer chain length, immobilized substrate surface concentration and surface charge. *Langmuir* **24,** 11762–11769 (2008).
18. Nagase, H. & Fields, G. B. Human matrix metalloproteinase specificity studies using collagen sequence-based synthetic peptides. *Peptide Sci.* **40,** 399–416 (1996).
19. Miller, M. A. *et al.* Proteolytic Activity Matrix Analysis (PrAMA) for simultaneous determination of multiple protease activities. *Integr. Biol.* **3,** 422–438 (2011).
20. Whitley, M. J. *et al.* A mouse-human phase 1 co-clinical trial of a protease-activated fluorescent probe for imaging cancer. *Sci. Transl. Med.* **8,** 320ra4 (2016).
21. Desnoyers, L. R. *et al.* Tumor-specific activation of an EGFR-targeting probody enhances therapeutic index. *Sci. Transl. Med.* **5,** 207ra144 (2013).
22. Miller, M. A. *et al.* Predicting therapeutic nanomedicine efficacy using a companion magnetic resonance imaging nanoparticle. *Sci. Transl. Med.* **7,** 314ra183 (2015).
23. Bertrand, N., Wu, J., Xu, X., Kamaly, N. & Farokhzad, O. C. Cancer nanotechnology: the impact of passive and active targeting in the era of modern cancer biology. *Adv. Drug Deliv. Rev.* **66,** 2–25 (2014).
24. Wilhelm, S. *et al.* Analysis of nanoparticle delivery to tumours. *Nat. Rev. Mater.* **1,** 16014 (2016).
25. Davis, M. E. *et al.* Evidence of RNAi in humans from systemically administered siRNA via targeted nanoparticles. *Nature* **464,** 1067–1070 (2010).
26. Hrkach, J. *et al.* Preclinical development and clinical translation of a PSMA-targeted docetaxel nanoparticle with a differentiated pharmacological profile. *Sci. Transl. Med.* **4,** 128ra39 (2012).
27. Ruoslahti, E. Specialization of tumour vasculature. *Nat. Rev. Cancer* **2,** 83–90 (2002).
28. Ruoslahti, E. & Bhatia, S. N. & Sailor, M. J. Targeting of drugs and nanoparticles to tumors. *J. Cell Biol.* **188,** 759–768 (2010).
29. Lin, K. Y., Kwon, E. J., Lo, J. H. & Bhatia, S. N. Drug-induced amplification of nanoparticle targeting to tumors. *Nano Today* **9,** 550–559 (2014).
30. Pang, H.-B. *et al.* An endocytosis pathway initiated through neuropilin-1 and regulated by nutrient availability. *Nat. Commun.* **5,** 4904 (2014).
31. Fogal, V., Zhang, L., Krajewski, S. & Ruoslahti, E. Mitochondrial/cell-surface protein p32/gC1qR as a molecular target in tumor cells and tumor stroma. *Cancer Res.* **68,** 7210–7218 (2008).
32. Dufour, A. *et al.* Small-molecule anticancer compounds selectively target the hemopexin domain of matrix metalloproteinase-9. *Cancer Res.* **71,** 4977–4988 (2011).

33. Zurawski, V. R. *et al.* An initial analysis of preoperative serum CA 125 levels in patients with early stage ovarian carcinoma. *Gynecol. Oncol.* **30,** 7–14 (1988).
34. Ren, Y., Hauert, S., Lo, J. H. & Bhatia, S. N. Identification and characterization of receptor-specific peptides for siRNA delivery. *ACS Nano* **6,** 8620–8631 (2012).
35. Drapkin, R. *et al.* Human epididymis protein 4 (HE4) is a secreted glycoprotein that is overexpressed by serous and endometrioid ovarian carcinomas. *Cancer Res.* **65,** 2162–2169 (2005).
36. Rankin, E. B. *et al.* AXL is an essential factor and therapeutic target for metastatic ovarian cancer. *Cancer Res.* **70,** 7570–7579 (2010).
37. Alper, Ö. *et al.* Epidermal growth factor receptor signaling and the invasive phenotype of ovarian carcinoma cells. *J. Natl Cancer Inst.* **93,** 1375–1384 (2001).
38. Brown, P. O. & Palmer, C. The preclinical natural history of serous ovarian cancer: defining the target for early detection. *PLoS Med.* **6,** e1000114 (2009).
39. Sugahara, K. N. *et al.* Tissue-penetrating delivery of compounds and nanoparticles into tumors. *Cancer Cell* **16,** 510–520 (2009).
40. Desgrosellier, J. S. & Cheresh, D. A. Integrins in cancer: biological implications and therapeutic opportunities. *Nat. Rev. Cancer* **10,** 9–22 (2010).
41. Yao, M., Lam, E. C., Kelly, C. R., Zhou, W. & Wolfe, M. M. Cyclooxygenase-2 selective inhibition with NS-398 suppresses proliferation and invasiveness and delays liver metastasis in colorectal cancer. *Br. J. Cancer* **90,** 712–719 (2004).
42. Jackson, B. C., Nebert, D. W. & Vasiliou, V. Update of human and mouse matrix metalloproteinase families. *Hum. Genomics* **4,** 194–201 (2010).
43. Sanman, L. E. & Bogyo, M. Activity-based profiling of proteases. *Annu. Rev. Biochem.* **83,** 249–273 (2014).
44. Withana, N. P. *et al.* Labeling of active proteases in fresh-frozen tissues by topical application of quenched activity-based probes. *Nat. Protoc.* **11,** 184–191 (2016).
45. Sugahara, K. N. *et al.* Coadministration of a tumor-penetrating peptide enhances the efficacy of cancer drugs. *Science* **328,** 1031–1035 (2010).
46. Van Gorp, T. *et al.* HE4 and CA125 as a diagnostic test in ovarian cancer: prospective validation of the Risk of Ovarian Malignancy Algorithm. *Br. J. Cancer* **104,** 863–870 (2011).
47. Alcázar, J. L., Guerriero, S., Laparte, C., Ajossa, S. & Jurado, M. Contribution of power Doppler blood flow mapping to gray-scale ultrasound for predicting malignancy of adnexal masses in symptomatic and asymptomatic women. *Eur. J. Obstet. Gynecol. Reprod. Biol.* **155,** 99–105 (2011).
48. Park, J.-H. *et al.* Systematic surface engineering of magnetic nanoworms for *in vivo* tumor targeting. *Small* **5,** 694–700 (2009).

Acknowledgements

We thank H. Fleming (MIT) for critical editing of the manuscript, and A. Warren (MIT), G. Kwong (Georgia Institute of Technology), J. Voog (MIT, Massachusetts General Hospital), V. Ramanan and C. Buss (MIT) for helpful discussion. We are grateful to the Koch Institute Swanson Biotechnology Core at MIT, especially S. Malstrom, K. Cormier and veterinary pathologist R. T. Bronson. This study was supported in part by a Koch Institute Support Grant P30-CA14051 from the National Cancer Institute (Swanson Biotechnology Center), a Core Center Grant P30-ES002109 from the National Institute of Environmental Health Sciences, the Ludwig Fund for Cancer Research, and the Koch Institute Marble Center for Cancer Nanomedicine. E.J.K. acknowledges support from the Ruth L. Kirschstein National Research Service Award (1F32CA177094-01). J.S.D. thanks the National Science Foundation Graduate Research Fellowship Program for support. S.N.B. is a Howard Hughes Institute Investigator.

Author contributions

E.J.K. and J.S.D. performed the experiments and analysed the data. E.J.K., J.S.D. and S.N.B. designed the experiments and wrote the manuscript.

Additional information

Supplementary information is available for this paper.

Reprints and permissions information is available at www.nature.com/reprints.

Correspondence and requests for materials should be addressed to S.N.B.

How to cite this article: Kwon, E. J., Dudani, J. S. & Bhatia, S. N. Ultrasensitive tumour-penetrating nanosensors of protease activity. *Nat. Biomed. Eng.* **1,** 0054 (2017).

Publisher's note: Springer Nature remains neutral with regard to jurisdictional claims in published maps and institutional affiliations.

Competing interests

The authors are listed as inventors on patent applications related to the content of this work.